Faraday Discussions

Accepted Manuscript

This manuscript will be presented and discussed at a forthcoming Faraday Discussion meeting. All delegates can contribute to the discussion which will be included in the final volume.

Register now to attend! Full details of all upcoming meetings: http://rsc.li/fd-upcoming-meetings

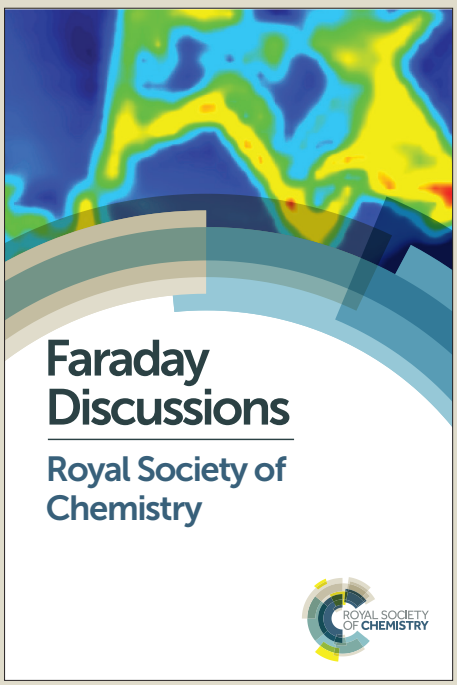

This is an *Accepted Manuscript*, which has been through the Royal Society of Chemistry peer review process and has been accepted for publication.

Accepted Manuscripts are published online shortly after acceptance, before technical editing, formatting and proof reading. Using this free service, authors can make their results available to the community, in citable form, before we publish the edited article. We will replace this *Accepted Manuscript* with the edited and formatted *Advance Article* as soon as it is available.

You can find more information about *Accepted Manuscripts* in the Information for Authors.

Please note that technical editing may introduce minor changes to the text and/or graphics, which may alter content. The journal's standard Terms & Conditions and the Ethical guidelines still apply. In no event shall the Royal Society of Chemistry be held responsible for any errors or omissions in this *Accepted Manuscript* or any consequences arising from the use of any information it contains.

ROYAL SOCIETY OF CHEMISTRY

www.rsc.org/faraday_d

CREATED USING THE RSC REPORT TEMPLATE (VER. 3.1) - SEE WWW.RSC.ORG/ELECTRONICFILES FOR DETAILS
Faraday Discussions
REVIEW www.rsc.org/xxxxxx | XXXXXXXX

First stages of siderite crystallisation during CO_2 corrosion of steel evaluated using *in-situ* synchrotron small- and wide- angle X-ray scattering.

Bridget Ingham[a,b], Monika Ko[b,c,d], Nick Laycock[e], Nigel M. Kirby[f], David E. Williams[b,d,*]
DOI: 10.1039/b000000x

We use *in-situ* synchrotron small- and wide-angle X-ray scattering (SAXS-WAXS) to demonstrate that the formation of crystalline siderite ($FeCO_3$) during the corrosion of steel in CO_2-saturated brine – a problem of practical interest relating to the growth of protective scales on the interior surface of oil and gas production pipelines – is preceded by the formation of a colloidal precipitate in the solution and an amorphous surface layer, both assumed to be amorphous ferrous carbonate. Grazing incidence SAXS shows instantaneous film formation upon the application of an anodic potential, followed by development of a separate population of particles at later times, then by the formation of crystalline species, observed by WAXS. These observations can be interpreted in terms of crystal nucleation within the amorphous surface layer. Traces of Cr^{3+} in the solution significantly accelerate the precipitation rate of the colloidal precursor and accelerate the appearance of the crystalline scale. We speculate on the significance of these observations for the nucleation, growth and morphology of the corrosion scale and hence its protectiveness.

1 Introduction

The dependence of nucleation and subsequent growth of crystalline surface scales is of particular importance in relation to the formation of corrosion scales that may be protective or not, according to their growth morphology. It connects to general questions about the precursor states for crystal nucleation onto surfaces from solution, and the dependence of crystal nucleation on supersaturation and on the presence of other solution species. Addressing this interesting and experimentally challenging question requires methods both for control of supersaturation and for measurement of crystal and precursor composition and size distribution through the stages of nucleation and growth[1, 2]. Small-angle X-ray scattering (SAXS) is a powerful technique for measuring the size distribution of particles (1-100 nm in size) in solution within a defined region of space. The high flux of synchrotron radiation allows the temporal evolution of the size distribution of nanoparticles to be followed[3] and the formation of amorphous precursor states for crystalline species to be studied[4]. A combination of small- and wide-angle X-ray scattering (SAXS-WAXS) allows the process of nucleation and growth of amorphous phases and their subsequent evolution into crystalline phases to be followed in great detail[5]. Grazing-incidence SAXS (GI-SAXS) [6] provides information about the development of surface films[7, 8] and nucleation on surfaces[9].

The particular system investigated here concerns the formation of corrosion scales which can be protective or otherwise depending on the growth morphology. In the case of corrosion of pipeline steels in hot brine saturated with carbon dioxide, the scale formed is siderite, $FeCO_3$. A highly crystalline, protective scale is often formed[10-12]. The magnitude of the corrosion rate and the occurrence or otherwise of localized corrosion ('mesa' corrosion) is determined by the nucleation, growth, morphology and stability of this scale[13-15]. In previous work using grazing incidence X-ray diffraction (XRD), we have demonstrated that there is a significant induction time from the start of anodic polarisation for the observation of crystalline siderite. The induction time is dependent on the solution and metal alloy composition, metal microstructure and surface roughness and the presence or otherwise of scale inhibitors[16-20]. Chukanovite, $Fe_2(OH)_2CO_3$ can also be formed[21-24], dependent on temperature and pH. It was noted that the critical supersaturation, S_{crit} , for the nucleation of crystalline siderite appears to be very high. The strong temperature dependence of the corrosion rate[11, 25, 26] can be related to the temperature dependence of S_{crit} and of the crystallisation rate[27], determining whether or not a protective scale is formed[28]. The development of predictive models for the corrosion rate requires estimated values for the rate of formation and growth of the scale, and methods for codifying the development of scale morphology. This in turn requires estimation of S_{crit} and crystallite growth rate. As noted by Remita *et al.* values given in the literature for the precipitation rate constant of siderite vary very widely, by a factor of 10^5 [29]. Literature on the value of S_{crit} for precipitation of siderite, and studies on the subsequent growth rate of the crystals formed, is limited[27, 30-32]. Sun and Nešić [30] measured the corrosion layer accumulation rates of siderite for values of supersaturation between 10 and 350. By adding an excess of iron to a CO_2-saturated solution and monitoring the system until precipitation ceased, then measuring the concentration of iron, the implication was that S_{crit} should be around 10 for a temperature of 80°C. Tomson et al.[32] measured concentration as a function of time when Fe^{2+} was slowly added to a CO_2-saturated solution. From the time of the onset of precipitation, they estimated S_{crit} around 3 at 55°C, in a solution that also contained Ca^{2+}. In the absence of Ca^{2+} at 55°C, the precipitation rate appeared to become very low at supersaturation less than about 10^2 [27]: in this work, the solutions were rigorously de-oxygenated to avoid the possible presence of Fe^{3+}. Remita *et al.*[29] discuss the importance of slow kinetics on siderite precipitation, and quote a supersaturation factor ($[Fe^{2+}]/[Fe^{2+}]_{eq}$) of around 7. Some of the discrepancies in the literature could be because the demonstrated effect of high-valent metal ions[18] could mean that the presence of traces of Fe^{3+} might be important. The apparent supersaturation for the formation of crystalline siderite on the electrode surface can be estimated from our previous work (see Discussion) and is unfeasibly large ($\approx 10^7$). The literature on the crystallisation of other carbonates from amorphous precursors offers a possible resolution.

Precipitation of other carbonates is known to involve polymer like pre-nucleation clusters and the formation of amorphous phases in solution as precursors to crystalline formation. In particular, amorphous calcium carbonate has been extensively characterised as a precursor to its crystalline forms [33-36]. Clarkson *et al.* [34] studied the spontaneous precipitation of calcium carbonate from aqueous solution under various conditions of supersaturation, temperature and presence/absence of inhibitor. They reported the formation of intermediate phases prior to detection of crystalline phases: homogenous precipitation of amorphous calcium carbonate

(ACC) was observed under high initial supersaturation while heterogeneous precipitation of hydrated calcium carbonate colloids was observed under low initial supersaturation. Decomposition of these intermediate phases could then result in the formation of the crystalline phase. Using synchrotron small angle X-ray scattering, Bolze *et al.* [4] demonstrated the formation of colloidal ACC particles in solution as a precursor to stable crystalline calcite. They noted a relatively constant mass density (or number of growing particles) following the nucleation period. Using a similar technique, Pontoni *et al.* [5] observed the transformation of these amorphous particles to crystals by dissolution and subsequent heterogeneous nucleation on the walls of their test container. Fernandez-Martinez *et al.* studied heterogeneous nucleation of $CaCO_3$ on mica[9]. In this case, ACC was not observed. Subsequent studies using levitated droplet techniques so that the only interface was a liquid-gas interface showed the formation of a stable, nanosized, liquid-like amorphous $CaCO_3$ phase that underwent a 'solution assisted transformation' to calcite [37]. A liquid-like phase was deduced as the form of the amorphous carbonate formed at high supersaturation, from which the crystals formed [38-40]. Such colloid particles have also been proposed as precursors in the precipitation of magnesium carbonate [41]. Similarly, amorphous ferrous carbonate (AFC) has been detected as a precursor to siderite [41, 42]. Sel *et al.* [41] measured the crystallisation kinetics of AFC in solution and reported a slow crystallisation process (the amorphous phase was persistent for at least 9 to 10 hours at 25°C following synthesis). These authors emphasised the need for rigorous removal of Fe^{3+} species. Hence it seems reasonable to propose that amorphous iron carbonate species in solution may act as precursors for the nucleation of both crystalline siderite and chukanovite.

In the present work, we have combined synchrotron (GI)-SAXS/WAXS with electrochemistry and demonstrate the delayed nucleation and growth of crystalline siderite following formation of a precursor amorphous film on a carbon steel electrode surface in CO_2-saturated brine at elevated temperature. We also demonstrate the formation of amorphous colloidal species in solution near a steel electrode and show the important effect of trace Cr^{3+} in solution on the precipitation rate of the amorphous species and on the transformation to crystalline siderite.

Experimental

The SAXS/WAXS beamline of the Australian Synchrotron[43] was used to conduct the experiments, which used two different setups. For the first, a purpose-built electrochemical cell with heating capability was used, which has been described previously for *in situ* X-ray diffraction experiments[16-18]. The cell has a reservoir at the top (volume 50 mL) into which the counter (Pt wire) and reference (Ag/AgCl) electrodes are placed, with a tapering neck at the base down to a narrow slot. The working electrode (a polished 1.5 mm diameter rod of carbon steel, embedded in epoxy resin) was mounted in the base of the slot. The slot depth above the working electrode was 1 mm. The beam (100 μm (h) × 240 μm (w) in size) intersected the electrode at grazing incidence but the incidence angle was ill-defined because the small size of the electrode meant that the surface was slightly rounded by polishing. The cell was periodically translated so that the beam either intersected the electrode surface or passed through the solution in the slot approximately 200 μm above the surface of the working electrode, in order to monitor the scattering signal from the

growing film and solution respectively. The positioning of the WAXS detector restricted the range of q_z observable in GI-SAXS. Here, $q = 4\pi \sin\theta / \lambda$ denotes the scattering vector: θ is half of the scattering angle with respect to the incident beam (the z direction is perpendicular to and xy parallel to the surface) and λ is the X-ray wavelength. The X-ray path length through the solution was approximately 2 mm. The electrochemical test solution was 0.5 M NaCl, and was saturated with CO_2 by bubbling of a stream of CO_2 gas at 1 bar. $CrCl_3$ was added to some solutions to a concentration of 10μM. The pH was adjusted to a calculated value of 6.8 at 80°C by adding 2 M NaOH in a 1:50 volume ratio. The solution was heated to 80 ± 1 °C. CO_2 was bubbled in the reservoir continuously throughout the experiment, and the cell was sealed to prevent oxygen ingress. The sample was first polarised at -1 V (vs. Ag/AgCl) for 5 minutes to reduce any residual surface oxide, then allowed to reach a steady state at open-circuit (5 minutes), then a potentiostatic or galvanostatic anodic current programme was applied. The exposure time was 10 s, with a 10 s pause between each position (i.e. the time between two measurements at the same position was 40 s). SAXS images were recorded using a Pilatus 1M detector, and WAXS images were collected simultaneously using a Pilatus 200k detector. The scans collected before the initiation of the anodic reaction were averaged and used as the background scattering.

A second experimental setup was used for direct injection of Fe^{2+} solution into CO_2-saturated 0.5 M NaCl. A syringe was connected to a stepper motor to allow remote control of the injection while data were being collected. $FeSO_4$ solution (50 mM in 0.5 M NaCl) freshly prepared in nitrogen-degassed MilliQ® water was injected at 1.7 μL.s^{-1} through a 20nm filter[†] into 200 mL of 0.5 M NaCl inside a temperature-controlled vessel with CO_2 continuously bubbling. A peristaltic pump was used to continuously extract solution to be passed through a 2 mm diameter quartz capillary for sampling by the X-ray beam, after which it returned to the vessel. SAXS images were continuously recorded with an exposure time of 1 s. Scans were averaged together in groups of 10. A series of static solutions of different Fe^{2+} concentrations were measured in a similar manner to determine the effect of Fe^{2+} ions on the solution scattering.

For all experiments, the X-ray energy was 15 keV (λ = 0.8266 Å) and the sample-detector distance was 7280 mm, calibrated using silver behenate. Data were processed using the ScatterBrain software (Australian Synchrotron), normalized to the intensity recorded at the beamstop and calibrated to the scattering of water. The background scattering from the solution and the cell windows was subtracted, then fitting was performed over the range $0.004 < q < 0.1$ Å^{-1} using the Irena 'Modeling II' macros[44].

Results

1. Concurrent SAXS and WAXS measurement shows that a colloidal species is formed above the electrode in advance of a crystalline deposit on the electrode, with characteristics altered by the presence of Cr(III) in solution

[†] Ferrous sulphate solutions are not stable and if left standing will develop a precipitate detectable by SAXS at a rate dependent on concentration: slow at 5mM but relatively rapid at 50mM.

Figure 1 shows SAXS from the X-ray beam passing through the solution above the steel electrode surface, and WAXS when the beam intersected the electrode surface, for a potentiostatic experiment (E = -500mV Ag/AgCl) in 0.5M NaCl, pH=6.8 at 80°C with continuous CO_2 bubbling. The beam passing above the electrode detected a species with size scale 10 nm (observable as a broad peak centred around q = 0.01 Å^{-1}) within 20 s from when the electrode potential stepped from the rest potential. The formation of crystalline siderite and chukanovite on the surface occurred at significantly later times. The SAXS and WAXS data were fitted and the results are plotted on the same time scale axis as the electrochemical current density in Figure 2. The SAXS data in Figure 1a were fitted using two populations of scatterers having log-normal distributions. The first had the total volume, mean radius, and standard deviation as fitted parameters (the standard deviation was constrained to be ≤0.8), while the second had the mean radius fixed at 135 nm and the standard deviation fixed at 0.5 – only the total volume was fitted. Attempts to fit the data using a single population failed. The first population of particles detected above the electrode surface, which may exist either in the solution or on the cell windows, formed with an average radius 15 nm which remained approximately constant during the period before the crystalline phase was observed, then started to rise (Figure 2b). The total volume of particles detected increased monotonically with time. The main peak of each phase in the WAXS patterns in Figure 1b was fitted as in our previous studies[16-18] to obtain the peak area, which is proportional to the volume of crystalline material (Figure 2a).

The results are consistent with earlier work[16-18, 45] given that the acceleration and deceleration of the cell during its translation might induce some convection, to which the ~~nucleation~~ of crystalline scale is sensitive[45]. The current density was initially high and relatively constant for an 'induction period' of around 30 minutes before it started to increase. During this induction period, the electrode surface is being roughened[16, 45]. Crystalline siderite was observed after a significant delay and its formation rate increased as the current rose. Chukanovite was observed as a minority phase that formed after the siderite film began to form. The current peaked and then dropped to a lower value than the initial current density, indicating an approach to passivation[16]. The siderite growth curve passed through a point of inflection at the current peak, indicating the approach to the plateau shown previously[16].

Figures 3 and 4 show the effect of addition of 10μM Cr^{3+} to the solution. Figure 3 shows that, in contrast to the result of Figure 1, the onset of scattering from above the electrode was delayed after the potential step that initiated the experiment. Crystalline species were observed on the electrode earlier than in the absence of Cr^{3+}. The SAXS data in Figure 3a were fitted using two populations of scatterers having log-normal distribution. The standard deviations were fixed at 0.3 for the larger scatterers, which emerged first, and 0.8 for the smaller scatterers, which became dominant at later times. The total volume of particles and the mean radii of these distributions were fitted parameters. Attempts to fit the data using a single population failed. These, together with the peak area of the main peak of each phase in the WAXS patterns (Figure 3b) and the electrochemical current density, are plotted on the same time axis in Figure 4. The scattering species, though of similar or smaller size to those observed in the absence of Cr^{3+}, grew steadily even before the onset of crystallisation.

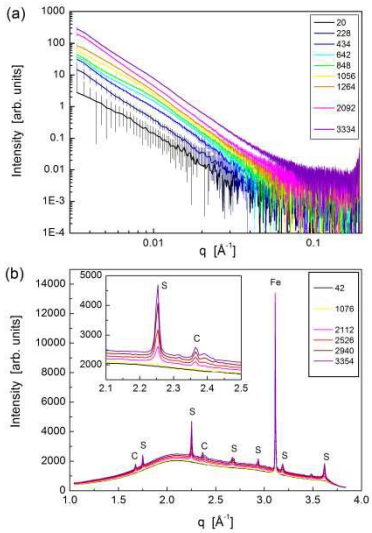

Figure 1. *In situ* snapshots at selected times, as indicated (in seconds), of raw data collected during an electrochemical experiment with CO_2-saturated 0.5 M NaCl at pH=6.8 at 80°C under potentiostatic control at -500 mV (vs. Ag/AgCl). (a) SAXS with the beam passing above the electrode and (b) WAXS with the beam intersecting the electrode. The solution signal prior to applying the potential was subtracted from the SAXS data as a background. For the WAXS data, peaks corresponding to siderite ($FeCO_3$) and chukanovite ($Fe_2(OH)_2CO_3$) are labelled as 'S' and 'C' respectively, along with that from the Fe electrode.

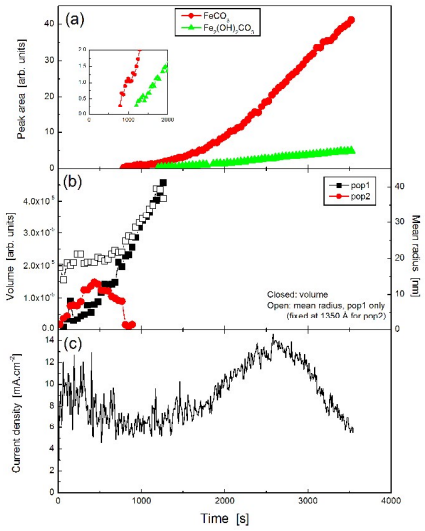

Figure 2. Derived results from figure 1 for an electrochemical experiment with CO_2-saturated 0.5 M NaCl at pH=6.8 at 80°C under potentiostatic control at -500 mV (vs. Ag/AgCl): (a) WAXS peak area for the most intense peak of each phase. The inset shows the development at the early stages, locating the initiation time for the crystalline phases; (b) SAXS fitting parameters (the mean radius for pop2 is fixed and so not plotted); (c) electrochemical current density.

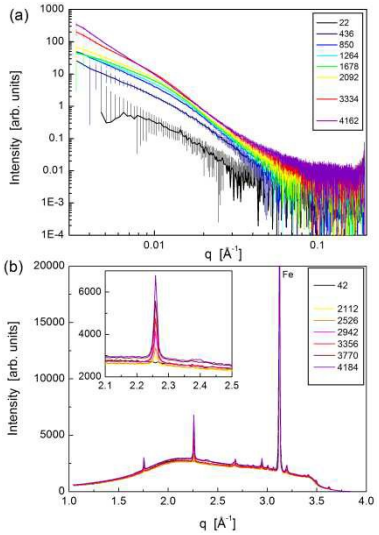

Figure 3. *In situ* snapshots at selected times, as indicated (in seconds), of (a) SAXS and (b) WAXS raw data collected during an electrochemical experiment with CO_2-saturated 0.5 M NaCl with 10 µM $CrCl_3$ at pH=6.8 at 80°C under potentiostatic control at -500 mV (vs. Ag/AgCl). The solution signal prior to applying the potential was subtracted from the SAXS data as a background. For the WAXS data, peaks corresponding to siderite ($FeCO_3$) and chukanovite ($Fe_2(OH)_2CO_3$) are labelled as 'S' and 'C' respectively, along with the Fe electrode.

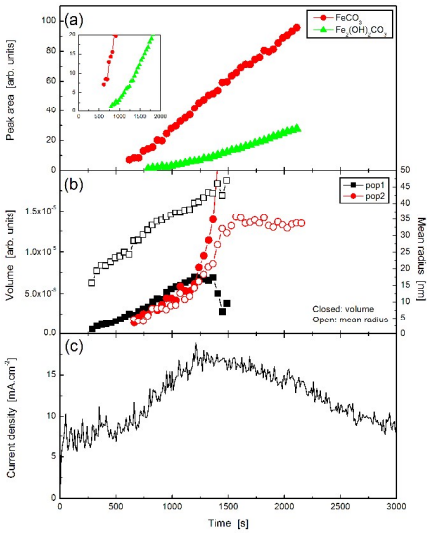

Figure 4. Derived results from figure 3 for an electrochemical experiment with CO_2-saturated 0.5 M NaCl with 10 µM $CrCl_3$ at pH=6.8 at 80°C under potentiostatic control at -500 mV (vs. Ag/AgCl): (a) WAXS peak area for the most intense peak of each phase. The inset shows the development at the early stages, locating the initiation time for the crystalline phases; (b) SAXS fitting parameters for the two log normal distribution populations; (c) electrochemical current density.

Again, the results are consistent with previous work[18]. The current rise corresponded to the nucleation of crystalline siderite onto the electrode surface. The induction time before observation of the current rise and the formation of siderite was significantly shortened in the presence of Cr^{3+}. Chukanovite was observed as a minority phase nucleating after siderite. In contrast to the shortened timescale for the observation of siderite on the electrode surface, there was a delay to the observation of particles above the electrode. Again these particles had an initial size of around 15 nm. They were observed shortly before the detectable nucleation of crystalline siderite, and increased in total volume and radius steadily over time. The volume of the smaller population (having a broad size distribution) rapidly increased after 1500 s (the peak time for the current density) but this may simply indicate that the overall size distribution was becoming increasingly broad, not that a separate population of particles was developing.

2. GI-SAXS shows the formation of an amorphous thin film on the electrode preceding crystallisation

Figure 5 shows grazing incidence (GI-SAXS) patterns measured with the X-ray beam intersecting the electrode surface, for the electrochemical experiment with CO_2-saturated 0.5 M NaCl at pH=6.8 at 80°C under potentiostatic control at -500 mV (vs. Ag/AgCl). The specular reflection is the vertical streak in the image above the beamstop. Figures 6a and 6b show the time variation of the intensity along a cut through the pattern at fixed q_z (indicated by the dotted lines in Fig. 5), and compares the development of the pattern with that observed in the presence of 10 μM Cr^{3+} in the solution (Figures 6c and 6d). The GISAXS intensity at a fixed q_z corresponds to scattering from objects of a particular size in the direction perpendicular to the electrode surface, e.g. particle height, cavity depth, or film thickness. The lateral scattering corresponds to the size of the scattering objects in plane, parallel to the electrode surface. The initial intense scattering in Figure 6a,c up to $q_{xy} \sim 10^{-3}$ Å^{-1} (black squares in Figure 6b,d) corresponds to the specular reflectance. This decreases in intensity at later times. At large q_{xy} (green triangles in Figure 6b,d), the data resemble a Guinier scattering pattern at later times corresponding to scattering objects approximately 7 nm in radius. This shows the effect of the nucleation of the crystalline film, which is evidenced by the emergence of diffraction peaks in the WAXS (blue inverted triangles in Figure 6b,d). In the absence of Cr^{3+} in the solution, the specular reflection first increased, approximately to a plateau, and then decreased. At intermediate q_{xy} (red circles in Figure 6b, the smallest q_{xy} at which lateral scattering can reliably be distinguished from changes in the specular reflection; size scale, $q^{-1} \approx 20$ nm) there was a plateau that corresponded to that observed in the specular reflection, followed by a further increase then a decrease preceding the formation of the crystalline deposit. At large q_{xy}, the scattering at longer time tracked the formation of the crystalline layer. In the presence of Cr^{3+} in the solution the temporal variation was different (Fig 6d). Both the specular reflection and the scattering at intermediate q_{xy} rose on a similar timescale, to a maximum, before falling after the crystalline deposit was detected. Thus the temporal development of structures of a particular lateral size scale was significantly altered by the presence of Cr^{3+} in the solution.

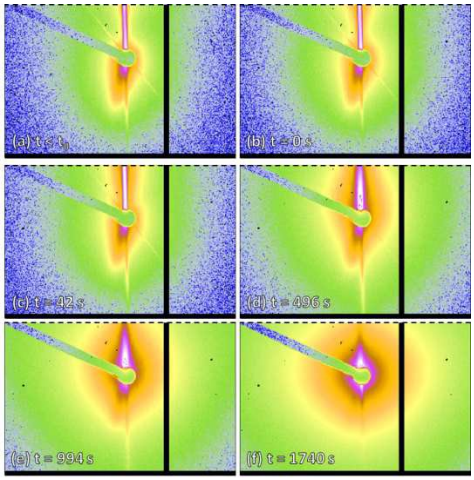

Figure 5. SAXS scans collected when the X-ray beam was striking the electrode, during an electrochemical experiment with CO_2-saturated 0.5 M NaCl at 80°C under potentiostatic control at -500 mV (vs. Ag/AgCl). The intense signal running vertically from the beam stop in the centre of the image is the specular reflection from the sample. The dotted line shows the cut at constant q_z along which intensity is plotted in Figure 6.

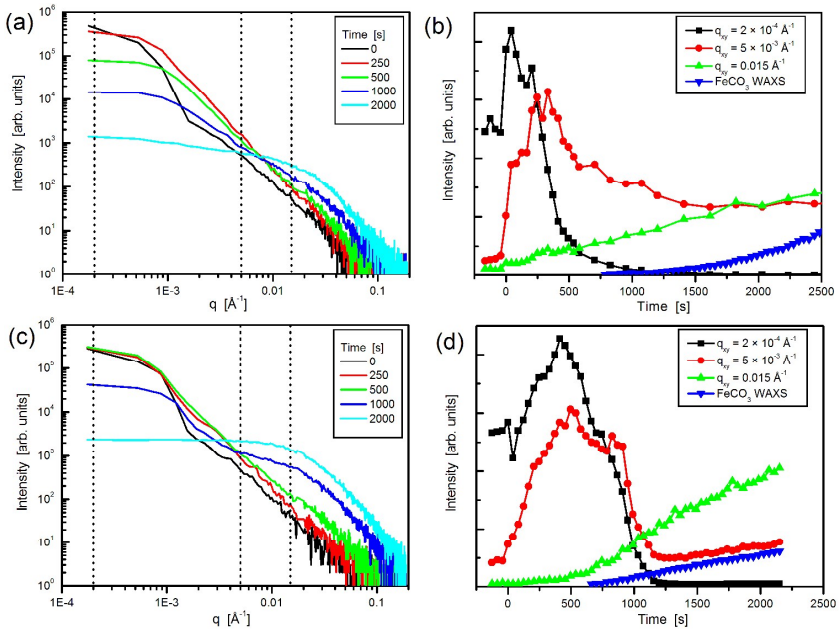

Figure 6. Analysis of GI-SAXS series from which selected scans are shown in Figure 5, showing (a, c)) intensity in q_{xy} along a cut at q_z = 0.0248 Å^{-1} and (b, d) Intensity as a function of time for three fixed (q_{xy}, q_z) points indicated by the black dotted lines in (a, c) respectively. The corresponding solution SAXS recorded when the beam was positioned above the electrode was subtracted for each time point. The behaviour in the absence (a,b) and presence (c,d) of 10µM Cr^{3+} in the solution is compared.

3. Galvanostatic step experiments show that both the precipitation rate and the growth rate of the colloidal species is increased in the presence of Cr(III) in the solution

Figure 7 shows the background-subtracted SAXS data and derived parameters with the beam position kept fixed passing above the electrode when the electrode was subject to a galvanostatic current stepping progressively to higher values. The behaviour in the absence and presence of Cr^{3+} in solution is compared. In the absence of Cr^{3+}, scattering corresponding to a mean particle radius of 25 nm (log-normal distribution with standard deviation 0.25 increasing to 0.8 with increasing time) was observed at the lowest current applied (55 µA cm^{-2}) after a delay of approximately 30-60s. Approximately 70 s after the step to 110 µA.cm^{-2} at t = 300 s, the total volume of particles started to increase steadily, but with little change in the particle size. In contrast, in the presence of 10 µM Cr^{3+}, no additional scattering above the background was detected before 250 s. Immediately after the step to 110 µA.cm^{-2} at 300 s, the mean particle size increased rapidly before stabilising at ≈60 nm. We develop in the Discussion the demonstration that the delay in appearance of particles above the electrode can be related to the critical supersaturation for nucleation of a precipitate and to the precipitation rate near the electrode, with a longer delay implying a greater precipitation rate or smaller critical supersaturation.

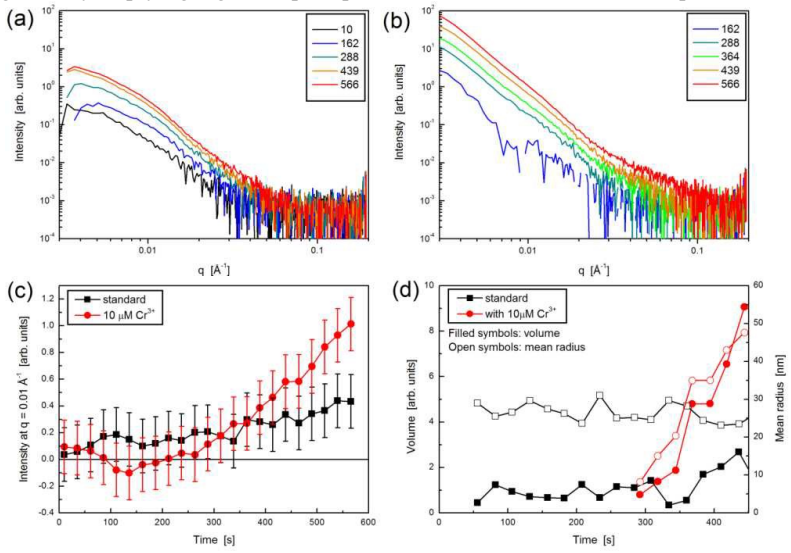

Figure 7. SAXS data collected from a current stepping experiment, from zero to 55 µA cm^{-2} at t = 0 then to 110 µA cm^{-2} at t = 300 s, with CO_2-saturated 0.5 M NaCl at 80°C in the absence (a) and presence (b)of Cr^{3+} in the solution , with the beam passing approximately 200 µm above the surface of the working electrode. The solution scan collected at open circuit before initiation of the current was subtracted as a background. The legend shows the time /s following the application of the current. (c) Location of the time of appearance of scattering species after the current step from zero at t =0, by plotting scattering at fixed q ; and (d) derived mean particle size and total volume of scattering species, comparing the behaviour in the absence and in the presence of 10µM Cr^{3+} in the solution.

4. A solution injection experiment demonstrates S_{crit} ≈2.5 for formation of a colloid

Figure 8 shows the increase of SAXS with time when a 50mM $FeSO_4$ solution was

slowly injected through a 20nm filter into rapidly stirred, CO_2-saturated 0.5M NaCl at pH 6.8 at 80°C. Above a threshold concentration of approximately 5 µM Fe^{2+}, located by extrapolating the concentration-dependence of the derived total volume of scattering species, two populations of scattering species were observed : one with a mean radius ≈ 4 nm, that increased with increase of Fe^{2+} concentration and the other of much larger particles (≈150 nm). SAXS of $FeSO_4$ solutions freshly prepared in deoxygenated water showed detectable particles of size scale >10 nm for solutions of concentration 5mM and above. From the onset Fe^{2+} concentration to observe particles, and knowing the solubility product K_{sp} and CO_3^{2-} concentration, we can estimate S_{crit} for the formation of a colloid:

$$S_{crit} = \frac{[Fe^{2+}][CO_3^{2-}]}{K_{sp}}$$

K_{sp} under these conditions is around 1.37×10^{-10} $mol^2.L^{-2}$ at 80°C [46]. The CO_3^{2-} concentration is estimated to be around 7×10^{-5} $mol.L^{-1}$ [20]. If the Fe^{2+} concentration at the onset of precipitation is around 5×10^{-6} $mol.L^{-1}$, this yields a value for S_{crit} of around 2.5.

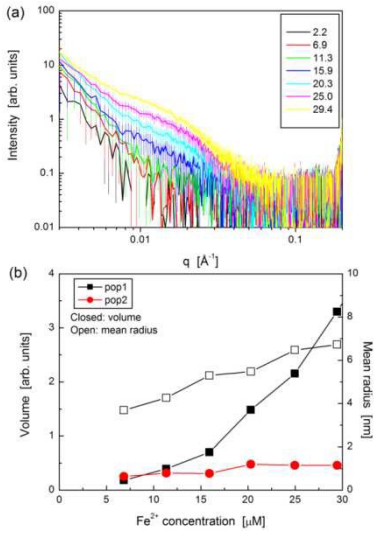

Figure 8. (a) SAXS data collected at various times during injection of a 50 mM $FeSO_4$ solution into 200 mL of a CO_2-saturated 0.5 M NaCl solution at 80°C at 0.1 mL/min. The legend shows the corresponding Fe^{2+} concentration in solution. The initial solution scan before injection commenced was subtracted as a background. (b) Derived mean particle radius and total volume of scattering species as a function of the Fe^{2+} concentration in solution. The mean radius of pop2 was fixed at 150nm

5. An interrupted galvanostatic measurement demonstrates heterogeneous nucleation of the colloid on the cell windows.

A current density of 0.56 $mA.cm^{-2}$ was applied for 1 minute, then turned off. After a further 10 minutes the current was turned on again. SAXS data were collected continuously through the experiment and are shown in Figure 9. A single population of scatterers having a log-normal distribution was used to fit the data. The mean

radius and total volume of particles were independent fitted parameters and are shown in Figure 9. Particles formed during the initial 1 min application of the current, having a mean radius of around 20 nm. During the period that the current was off, the total volume increased by a factor of three and the mean size increased by a factor of two. If the particles observed were forming in solution, one would expect the signal to decay during the 10 minutes that the current was turned off, as the particles either settled or diffused away. However, if they were forming on or adhering to the windows in the path of the X-ray beam, the signal would not change significantly (and may increase as Fe^{2+} concentration relaxed, or as an effect of X-ray exposure). The latter situation is what was observed here.

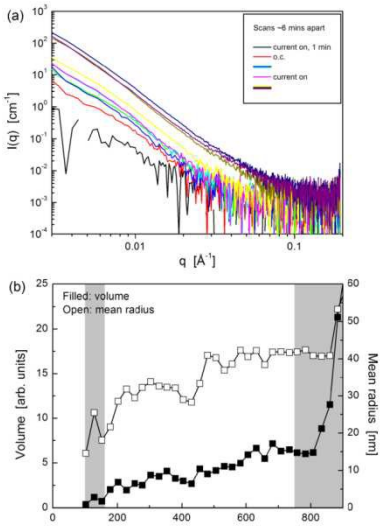

Figure 9. (a) SAXS data collected from an experiment with CO_2-saturated 0.5 M NaCl at 80°C where a galvanostatic current density of 0.56 mA.cm^{-2} was applied for 1 minute, turned off, and turned on again after 10 minutes. The initial solution scan before the current was first applied was subtracted as a background. (b) SAXS fitting parameters for the log normal distribution populations; the shaded areas show where the current was applied.

Discussion

The data are consistent with the formation and transformation of an amorphous, perhaps gel-like surface layer, which then gives way to crystalline species with kinetics significantly altered by the presence of Cr^{3+}. The ideas are consistent with Ostwald's 'rule of stages'[47, 48]. The data are consistent with the dissolution of the surface 'gel' layer leading to amorphous colloidal species both in solution and nucleating on other surfaces, with precipitation rate also significantly altered by the presence of Cr^{3+}. The discussion can be developed first from a consideration of the apparent supersaturation required for the nucleation of a crystalline surface film, then from analysis of the results of SAXS from the solution above the electrode and comparison with the supersaturation required to form amorphous species by injection of ferrous sulphate into the CO_2-saturated NaCl solution, and finally from consideration of the GI-SAXS results.

For the purpose of discussing the apparent supersaturation achieved in a

galvanostatic experiment, and the detection of precipitating species, Figure 10 illustrates results from an idealized diffusion geometry for the slot above the electrode: for the purpose of modeling, the experimental geometry (Figure 10a, inset, b) is approximated by the simple linear geometry (Figure 10a, inset, a). A constant current density is applied to cause dissolution of an electrode at the base of the slot. The precipitating reagent (CO_2) is present outside the slot at uniform concentration. The X-ray beam detects the formation of precipitate within a section of the slot above the electrode.

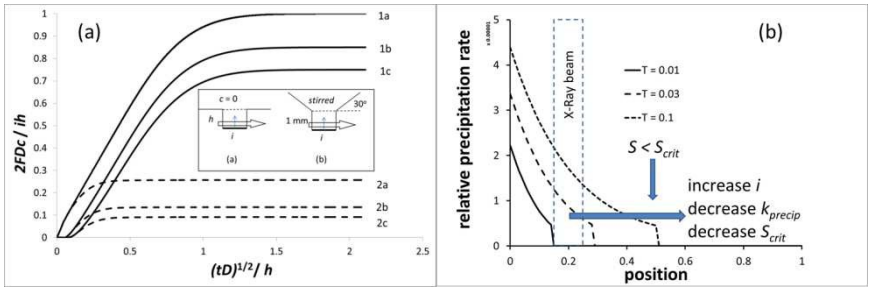

Figure 10 Results of finite difference solution of the diffusion problem for Fe^{2+} and CO_2 with siderite precipitation. (a) Time evolution of Fe^{2+} concentration with $K_p = 0$ (curve 1a at the electrode surface and 1b, 1c at positions corresponding approximately to the bottom and top of the X-ray beam) and K_p =20 (curves 2, at the electrode surface, bottom and top of the X-ray beam). The inset illustrates the experimental geometry, inset b, and the idealized calculation geometry, inset a. (b) Relative precipitation rate at different time $T = tD/h^2$ as a function of position above the electrode, calculated for $K_p = 20$ with flux $2Fic_0/(hD) = 10^{-5}$ and critical supersaturation $S^*_{scaled} = 10^{-3}$, corresponding approximately to the experimental conditions of figure 7 with $S_{crit} \approx 5$.

Ignoring the effects of hydrolysis of the metal ions, the reaction scheme for the precipitation of siderite can be written:

$$CO_2 + H_2O \underset{k_{-1}}{\overset{k_1}{\rightleftharpoons}} H_2CO_3$$

$$H_2CO_3 \overset{K_1}{\rightleftharpoons} H^+ + HCO_3^- \overset{K_2}{\rightleftharpoons} H^+ + CO_3^{2-}$$

$$Fe^{2+} + CO_3^{2-} \xrightarrow{k_2} FeCO_3$$

The discussion focuses on the attainment of the critical condition for precipitation, and hence considers the case when the CO_2 concentration is not greatly perturbed. In that case, the discussion is simplified by noting that $[CO_3^{2-}] << [HCO_3^-] + [H_2CO_3]$ and writing $[CO_3^{2-}] = \beta[CO_2]$ with β constant ($\approx 5.6\times10^{-3}$ at 80°C, pH 6.8). Then, ignoring migration in view of the excess of NaCl, the diffusion equation for Fe^{2+} and CO_2 can be written:

$$\frac{\partial C_{Fe^{2+}}}{\partial T} = \frac{\partial^2 C_{Fe^{2+}}}{\partial X^2} - K_p C_{Fe^{2+}} C_{CO_2}$$

$$\frac{\partial C_{CO_2}}{\partial T} = \frac{\partial^2 C_{CO_2}}{\partial X^2} - K_p C_{Fe^{2+}} C_{CO_2}$$

Where the scaled time, $T = tD/h^2$, position, $X = x/h$ and concentration $C = c/c_0$. Here, D denotes the diffusion coefficient of Fe^{2+} (2.1×10^{-5} cm^2 s^{-1} at 80°C), h is the depth of the slot (≈1 mm), c_0 is the saturation concentration of CO_2 (outside the slot; ≈0.013 M at 80°C and pH 6.8) and t is the time. The rate constant for consumption of Fe^{2+} through formation of siderite, $K_p = \beta k_2 K_2 h^2/D$ if the supersaturation, $S \geq S^*$, and =0 if $S < S^*$. In the scaled variables, the supersaturation, $S_{scaled} = C_{Fe^{2+}} C_{CO_3^{2-}} = SK_{sp}/\beta c_0^2$. Figure 10 shows results of a finite-difference solution of these equations with boundary conditions at the electrode of constant flux of Fe^{2+} and zero flux of CO_2, and at the top of the slot of $C_{Fe^{2+}} = 0$ and $C_{CO_3^{2-}} = 1$.

From the time to observe a crystalline product and the current density preceding the crystalline scale nucleation (~1500s, and ~6 mA cm^{-2}, Figure 1) if there were no precipitation preceding the crystalline scale then, from Figure 10a the approximate surface concentration of Fe^{2+} can be calculated (≈0.1 M) and hence the apparent supersaturation (≈ 10^7) which is physically unreasonable. The SAXS (Figures 1 and 2) detects the colloidal, amorphous precipitate which is indeed present and which precedes the crystallisation. The model is therefore of an induction time for crystallization from a preceding amorphous material. This induction time for crystallization from an amorphous precursor is evidently decreased in the presence of a small concentration of Cr^{3+} in the solution (Figures 3 and 4).

When precipitation is occurring, Figure 10b illustrates that a precipitation front would move out from the electrode surface, with a delay before the front moved through the position of the X-ray beam, as indeed was observed (Figure 7). We verified that the delay time for a given (low) current density was consistent with the critical supersaturation determined in the solution injection experiment (Figure 8). Figure 10b shows that, the higher the precipitation rate, the longer it takes for the precipitation front to reach the position of the X-ray beam and hence to give rise to detectable scattering. This calculation illustrates that the significant additional delay in appearance of precipitate in the X-ray beam caused by addition of trace Cr^{3+} to the solution is due to an increase in precipitation rate or a decrease in critical supersaturation. The SAXS experiment (Figure 4 and 7) also showed that the presence of trace Cr^{3+} in solution caused a significant increase in the growth rate of the amorphous colloidal particles initially formed.

Although the experimental setup was not ideal for GI-SAXS, the results are informative. The interpretation must take into account the development of surface roughness, previously demonstrated to occur during the induction period before the appearance of crystalline material[16, 45]. The fractal dimension of the diffraction ring (a useful measure of 'spottiness'[49]) increases over time and has been interpreted as due to the removal by dissolution of smaller grains of the metal, resulting in an increase in surface roughening over time[45, 49]. While the fractal dimension of the diffraction ring does not necessarily relate to a fractal dimension of the surface morphology, we note that the SAXS of a rough interface gives a power law dependence on q of diffuse scattering intensity, with exponent decreasing as fractal dimension increases. This effect will be superimposed upon effects associated with the development of surface layers. The results in the absence of added Cr^{3+} (Figure 6) show a clear temporal separation of three stages in the development of the surface

layer, corresponding to different lateral size scales. The first stage is the immediate increase of specular reflection to a plateau, followed by a steep drop in signal, Figure 6b. A surface layer of amorphous $FeCO_3$ would have a significantly smaller density than Fe and thus a significantly smaller X-ray reflectivity. Roughening of the surface will also cause a decrease in reflectivity. The steep drop in specular reflectivity therefore can be interpreted as due to the coverage of the surface by a continuous film of amorphous $FeCO_3$. The increase prior to this is clearly a consequence of the electrochemical polarisation. Given the magnitude of the initial current density, the critical supersaturation for amorphous $FeCO_3$ would be exceeded almost immediately. We therefore interpret the increase in specular reflection to be a consequence of multiple reflection and refraction of the X-rays caused by the presence of a discontinuous layer comprising 'blobs' of amorphous $FeCO_3$, which subsequently grow to spread over the surface and eventually cover it. The next phase is the appearance of a new set of scatterers with lateral size scale ≈ 20 nm, indicated by the change of scattering intensity at intermediate q_{xy}. That result could be interpreted as due to aggregation within the surface layer. Thus, the results indicate that the initial stage is the formation of a thin layer of amorphous ferrous carbonate on the electrode, within which crystalline siderite or chukanovite subsequently forms. Speculatively, these stages could be the spreading of patches of an amorphous gel-like layer until it covers the surface, concurrent with the development of lateral inhomogeneity and clusters within this layer, analogous to the prenucleation clusters[50] noted for example for solution precipitation of $CaCO_3$[51] then finally the nucleation and growth of crystals, which is signalled by the appearance of a crystalline diffraction pattern.

A gel-like AFC layer covering the steel surface would form a barrier that would control the initial current density, depending on the thickness (primarily) of this layer and also on its density, which would control its ionic conductivity. The effect of the presence of trace Cr^{3+} in the solution could be interpreted as a significant acceleration and overlapping of all three stages. A different morphology of the amorphous 'gel' as it nucleates and spreads over the surface could account for the different temporal development of the specular reflectance. The development of lateral inhomogeneity and clusters within the gel layer would seem to have been significantly affected, such that the development of lateral inhomogeneity preceding crystal nucleation overlapped in time with the spreading and thickening of the gel layer that is presumed to be present.

Figure 11 gives a schematic model of the evolution of the surface state deduced from both the present and previous work. Important effects of surface roughness on the time scale for nucleation of crystalline phases have been observed, including in synchrotron experiments where the dominant effect on mass-transport to the surface should be the depth of the narrow slot above the electrode[45]. The idea of a secondary boundary layer, defined by the gel layer, helps understand these effects in that crystallisation would be controlled by the conditions specifically pertaining within the gel and thus sensitive to the local geometry and environment. The current rise upon nucleation of crystalline siderite, interpreted previously in terms of a local pH decrease[17], can with the new observations be interpreted in part as due to the development of holes in the amorphous surface layer as it transforms into a crystalline layer. By analogy with the transformation of amorphous to crystalline calcium carbonate[52], the transformation of hydrated AFC to crystalline siderite should result in a significant decrease in volume which would cause the AFC layer

locally to become thinner or be punctured. This model offers an alternative explanation for current rise upon crystallisation, whereby the presence of voids in the otherwise continuous AFC layer would decrease the potential drop across the surface layer and result in a rise in current density. Once the crystalline phases are formed, rapid growth of these materials may cause further acidification of the local solution due to the consumption of carbonate species, as previously proposed[17].

The transformation of AFC to crystalline phases is known to be strongly time dependent and slow[41]. The crystallisation process may be dependent on a number of factors, including the concentration of Fe^{2+} within the AFC layer as indicated in Scheme 1 below. Chukanovite is also a crystallisation product, and the relative amounts of chukanovite and siderite have proven in previous work to be somewhat variable[45]. The observation of an amorphous surface gel layer and the hypothesis that crystalline species nucleate within the gel layer can aid interpretation. Since in the electrochemical experiments iron is dissolving through the surface layer, there would be an iron excess present within the layer. Then, there would be the possibility of formation of a hydrated, iron-excess gel that could resemble amorphous chukanovite:

$$FeCO_3 \text{ (amorphous)} + Fe^{2+} + 2H_2O = Fe_2(OH)_2CO_3 \text{ (amorphous)} + 2H^+$$

Given that, there is the possibility of multiple transformation pathways as indicated in Scheme 1.

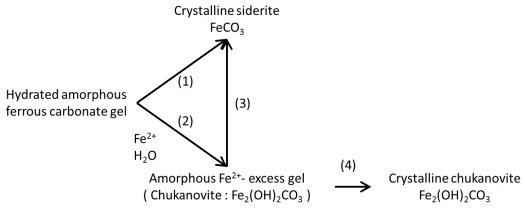

Scheme 1: Possible transformation paths to different crystalline products

In summary, this work taken with previous studies has shown that the nucleation and growth characteristics of crystalline siderite scales are unusual and that there is a complex inter-dependent relationship between the precipitation rate, the composition and the morphology of the formed scale. The important fact seems to be that direct formation of crystalline siderite from solution requires a very large critical supersaturation or a long induction time for nucleation. The formation of crystalline siderite is preceded by the formation of an amorphous colloidal ferrous carbonate (AFC) precipitate. The presence of Cr^{3+} in the solution has a significant effect on the precipitation and growth rate of AFC and on the crystallisation rate. As noted before, this phenomenon explains the very strong effect of small alloying additions of Cr in the steel in promoting the formation of thin but adherent and protective crystalline siderite scales. The crystalline layer is proposed to nucleate within an amorphous gel layer, whose thickness and composition may be dependent on the current density and surface boundary layer. In view of the known influence of a wide range of solution species on the nucleation and crystallisation of other carbonates, important effects of such species on the formation of crystalline siderite

scales and hence corrosion rate of steel in CO_2 environments, is to be expected. Given the demonstrated influence of the presence of high-valent metal ions, the effect of traces of Fe^{3+} might also be significant.

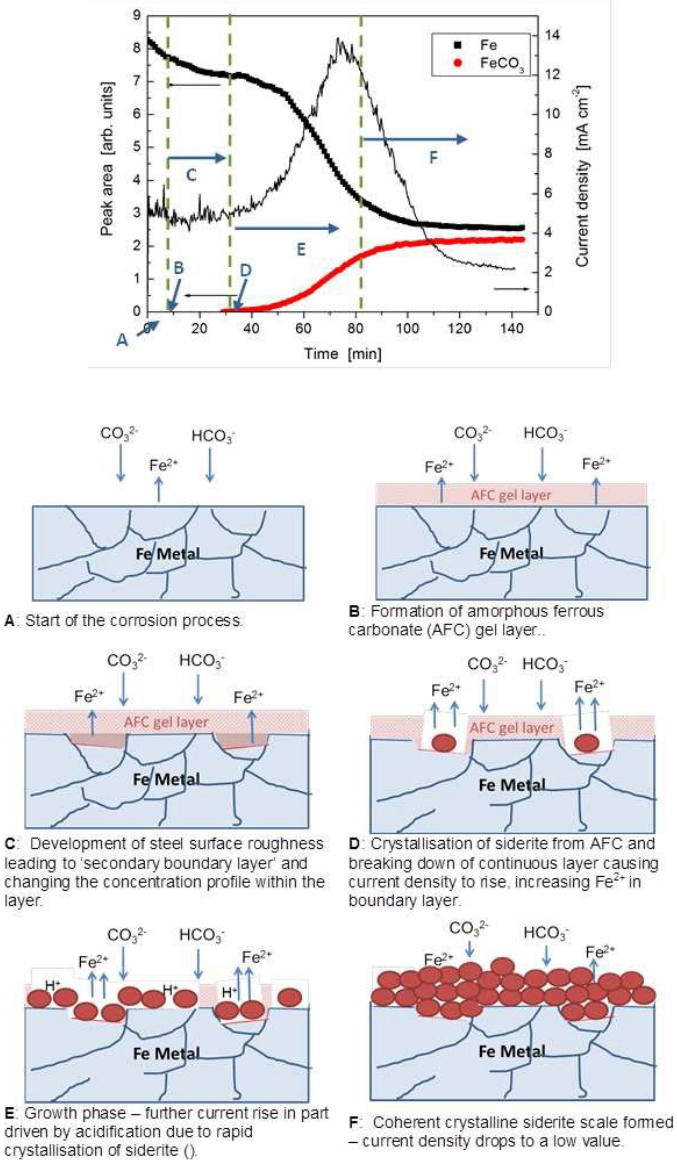

Figure 11: Schematic scale precipitation model during CO_2 corrosion of carbon steel, relating the different stages to the evolution of the current density (light line) and the diffraction pattern (heavy lines) observed from species on the surface (top panel from ref.[17].).

One final point to note is that the electrochemical experiments generally resulted in formation of friable scales with relatively small crystallite size. In contrast, open

circuit corrosion studies show scales comprising large, well-formed crystals. The discussion above implies that the conditions within a surface gel are critical for at least the initial development of a crystalline scale. In particular, the current density would determine the local supersaturation of Fe^{2+}, which would be significantly lower at open-circuit than that in the electrochemical experiments. A reasonable presumption is that, if the current density were high enough, the scale would be formed by the continuous nucleation of new, small crystals. In contrast, if the current density were low, the growth of crystallites might be expected to dominate.

Conclusions

The present work supports a model for CO_2 corrosion of pipeline steels in which corrosion-protective siderite scales nucleate within a thin surface 'gel' of amorphous iron carbonate. The precipitation rate of the amorphous carbonate is strongly increased as a consequence of the presence of Cr^{3+} in solution. The crystallisation rate of siderite from the amorphous precursor is also strongly increased in the presence of Cr^{3+}. We suggest that the conditions within a secondary boundary layer defined by the surface roughness and the current density determine the thickness of the surface gel and the subsequent crystallisation.

Acknowledgements

This work was funded by the New Zealand Ministry of Business, Innovation and Employment (MBIE) under contract C08X1003. Portions of this research were undertaken on the SAXS/WAXS beamline at the Australian Synchrotron, Victoria, Australia. We thank the New Zealand Synchrotron Group Ltd. for a grant to construct the electrochemical cell. We also thank Nick Birbilis (Monash University) for his generous advice and loan of equipment.

References

[a] *Callaghan Innovation, P.O. Box 31310, Lower Hutt 5040, New Zealand; E-mail: bridget.ingham@callaghaninnovation.govt.nz*
[b] *MacDiarmid Institute for Advanced Materials and Nanotechnology, Victoria University of Wellington, P.O. Box 600, Wellington 6140, New Zealand;*
[c] *Quest Integrity Group, P.O. Box 38096, Lower Hutt 5040, New Zealand*
[d] *School of Chemical Sciences, University of Auckland, Private Bag 92029, Auckland 1022, New Zealand; Email: david.williams@auckland.ac.nz*
[e] *College of Engineering and Physical Sciences, University of Birmingham, Edgbaston, Birmingham B15 2TT, U.K.*
[f] *Australian Synchrotron, 800 Blackburn Road, Clayton, VIC 3168, Australia*

1. O. Devos, C. Gabrielli, M. Tlili and B. Tribollet, *Journal of The Electrochemical Society*, 2003, **150**, C494-C501.
2. C. Gabrielli, G. Maurin, G. Poindessous and R. Rosset, *Journal of Crystal Growth*, 1999, **200**, 236-250.

3. B. Ingham, T. H. Lim, C. J. Dotzler, A. Henning, M. F. Toney and R. D. Tilley, *Chem. Mat.*, 2011, **23**, 3312-3317.
4. J. Bolze, B. Peng, N. Dingenouts, P. Panine, T. Narayanan and M. Ballauff, *Langmuir*, 2002, **18**, 8364-8369.
5. D. Pontoni, J. Bolze, N. Dingenouts, T. Narayanan and M. Ballauff, *Journal of Physical Chemistry*, 2003, **107**, 5123-5125.
6. G. Renaud, R. Lazzari and F. Leroy, *Surf. Sci. Rep.*, 2009, **64**, 255-380.
7. G. Kaune, M. A. Ruderer, E. Metwalli, W. Wang, S. Couet, K. Schlage, R. Röhlsberger, S. V. Roth and P. Müller-Buschbaum, *ACS Applied Materials & Interfaces*, 2008, **1**, 353-360.
8. P. Müller-Buschbaum, in *Applications of Synchrotron Light to Scattering and Diffraction in Materials and Life Sciences*, Springer, 2009, pp. 61-89.
9. A. Fernandez-Martinez, Y. D. Hu, B. Lee, Y. S. Jun and G. A. Waychunas, *Environmental Science & Technology*, 2013, **47**, 102-109.
10. M. H. Nazari, S. R. Allahkaram and M. B. Kermani, *Materials & Design*, 2010, **31**, 3559-3563.
11. M. B. Kermani and A. Morshed, *Corrosion*, 2003, **59**, 659-683.
12. A. Morshed, PhD thesis, University College London, 2002.
13. R. Nyborg and A. Dugstad, in *Paper no. 3642, CORROSION/2003* NACE International, 2003.
14. R. Nyborg, in *Paper No. 48, CORROSION/98*, NACE International, 1998.
15. W. Sun, S. Nesic and R. C. Woollam, *Corrosion Science*, 2009, **51**, 1273-1276.
16. B. Ingham, M. Ko, G. Kear, P. Kappen, N. Laycock, J. A. Kimpton and D. E. Williams, *Corrosion Science*, 2010, **52**, 3052-3061.
17. B. Ingham, M. Ko, N. Laycock, J. Burnell, P. Kappen, J. A. Kimpton and D. E. Williams, *Corrosion Science*, 2012, **56**, 96-104.
18. M. Ko, B. Ingham, N. Laycock and D. E. Williams, *Corrosion Science*, 2014, **80**, pp 237-246.
19. M. Ko, B. Ingham, N. Laycock and D. E. Williams, *Corrosion Science*, 2014, DOI:10.1016/j.corsci.2014.1010.1010.
20. M. Ko, N. J. Laycock, B. Ingham and D. E. Williams, *Corrosion*, 2012, **68**, 1085-1093.
21. R. De Marco, Z.-T. Jiang, B. Pejcic and E. Poinen, *Journal of The Electrochemical Society*, 2005, **152**, B389.
22. I. Azoulay, C. Remazeilles and P. Refait, *Corrosion Science*, 2012, **58**, 229-236.
23. P. Refait, J. A. Bourdoiseau, M. Jeannin, D. D. Nguyen, A. Romaine and S. Sabot, *Electrochimica Acta*, 2012, **79**, 210-217.
24. C. Rémazeilles and P. Refait, *Polyhedron*, 2009, **28**, 749-756.
25. M. Honarvar Nazari, S. R. Allahkaram and M. B. Kermani, *Materials & Design*, 2010, **31**, 3559-3563.
26. C. D. Waard and U. Lotz, in *A Working Party Report on Predicting CO_2 Corrosion in the Oil and Gas Industry*, The Institute of Materials, UK, 1994, p. 30.
27. S. Yean, H. A. Alsaiari, A. T. Kan and M. B. Tomson, SPE International Oilfield Scale Conference, 2008.
28. A. Dugtad, in *Paper No. 14, CORROSION/92*, NACE International, 1992.
29. E. Remita, B. Tribollet, E. Sutter, F. Ropital, X. Longaygue, J. Kittel, C. Taravel-Condat and N. Desamaise, *Journal of The Electrochemical Society*, 2008, **155**, C41-C45.
30. W. Sun and S. Nesic, *Corrosion*, 2008, **64**, 334-346.
31. M. L. Johnson and M. B. Tomson, in *Paper No. 268, CORROSION/91*, NACE International, 1991.
32. H. A. Alsaiari, A. Kan and M. Tomson, *SPE Journal*, 2010, **15**, 294-300.
33. D. Gebauer, A. Völkel and H. Cölfen, *Science*, 2008, **322**, 1819-1822.

34. J. R. Clarkson, T. J. Price and C. J. Adams, *J. Chem. Soc. Faraday Trans.*, 1992, **88**, 243-249.
35. H. Elfil and H. Roques, *AIChE*, 2004, **50**, 1908-1916.
36. F. C. Meldrum and R. P. Sear, *Science*, 2008, **322**, 1802-1803.
37. S. E. Wolf, J. Leiterer, M. Kappl, F. Emmerling and W. Tremel, *Journal of Americal Chemical Society*, 2008, **130**, 12342–12347.
38. A. F. Wallace, L. O. Hedges, A. Fernandez-Martinez, P. Raiteri, J. D. Gale, G. A. Waychunas, S. Whitelam, J. F. Banfield and J. J. D. Yoreo, *Science*, 2013, **341**, 885.
39. A. Myerson and B. Trout, *Science*, 2013, **341**, 855.
40. A. Accardo, M. Burghammer, E. D. Cola, M. Reynolds, E. D. Fabrizio and C. Riekel, *Langmuir*, 2011, **27**, 8216-8222.
41. O. Sel, A. V. Radha, K. Dideriksen and A. Navrotsky, *Geochimica et Cosmochimica Acta*, 2012, **87**, 61-68.
42. C. Jimenez-Lopez and C. S. Romanek, *Geochimica et Cosmochimica Acta*, 2004, **68**, 557-571.
43. N. M. Kirby, S. T. Mudie, A. M. Hawley, D. J. Cookson, H. D. T. Mertens, N. Cowieson and V. Samardzic-Boban, *J. Appl. Crystallogr.*, 2013, **46**, 1670-1680.
44. J. Ilavsky and P. R. Jemian, *J. Appl. Crystallogr.*, 2009, **42**, 347-353.
45. M. Ko, B. Ingham, N. Laycock and D. Williams, *Corrosion Science*, 2014, DOI: 10.1016/j.corsci.2014.1010.1010.
46. W. Sun, S. Nešić and R. C. Woollam, *Corrosion Science*, 2009, **51**, 1273-1276.
47. J. Nyvlt, *Cryst. Res. Technol.*, 1995, **30**, 443-449.
48. R. Van Santen, *The Journal of Physical Chemistry*, 1984, **88**, 5768-5769.
49. B. Ingham, *J. Appl. Crystallogr.*, 2014, **47**, 166-172.
50. D. Gebauer, M. Kellermeier, J. D. Gale, L. Bergstrom and H. Coelfen, *Chemical Society Reviews*, 2014, **43**, 2348-2371.
51. D. Gebauer, A. Volkel and H. Colfen, *Science*, 2008, **322**, 1819-1822.
52. J. Ihli, W. C. Wong, E. H. Noel, Y.-Y. Kim, A. N. Kulak, H. K. Christenson, M. J. Duer and F. C. Meldrum, *Nat Commun*, 2014, **5**.